JVST A
Journal of Vacuum Science & Technology A

ARTICLE

pubs.aip.org/avs/jva

Over 6 MV/cm operation in β-Ga_2O_3 Schottky barrier diodes with IrO_2 and RuO_2 anodes deposited by molecular beam epitaxy

Cite as: J. Vac. Sci. Technol. A 42, 033206 (2024); doi: 10.1116/6.0003468
Submitted: 17 January 2024 · Accepted: 7 March 2024 ·
Published Online: 10 April 2024

B. Cromer,[1,a] D. Saraswat,[1,b] N. Pieczulewski,[1] W. Li,[2,c] K. Nomoto,[2] F. V. E. Hensling,[1] K. Azizie,[1] H. P. Nair,[1] D. G. Schlom,[1,3,4] D. A. Muller,[5] D. Jena,[1,2,3] and H. G. Xing[1,2,3,d]

AFFILIATIONS

[1]Department of Materials Science and Engineering, Cornell University, Ithaca, New York 14853
[2]School of Electrical and Computer Engineering, Cornell University, Ithaca, New York 14853
[3]Kavli Institute at Cornell, Cornell University, Ithaca, New York 14853
[4]Leibniz-Institut fur Kristallzuchtung Max-Born-Strasse 2, 12849 Berlin, Germany
[5]School of Applied and Engineering Physics, Cornell University, Ithaca, New York 14853

Note: This paper is part of the Special Topic Collection on Gallium Oxide Materials and Devices.
[a]**Author to whom correspondence should be addressed:** bjc326@cornell.edu
[b]**Current address:** Materials Science and Engineering, Stanford University, Stanford, CA 94305.
[c]**Current address:** Intel, Santa Clara, CA 95054.
[d]**Electronic mail:** grace.xing@cornell.edu

ABSTRACT

β-Ga_2O_3 is actively touted as the next ultrawide bandgap material for power electronics. To fully utilize its high intrinsic critical electric field, development of high-quality robust large-barrier height junctions is essential. To this end, various high-work function metals, metal oxides, and hole-conducting oxides have been deposited on Ga_2O_3, primarily formed by sputter deposition. Unfortunately, reports to date indicate that measured barrier heights often deviate from the Schottky–Mott model as well as x-ray photoelectron spectroscopy (XPS) extractions of conduction band offsets, suggesting significant densities of electrically active defects at these junctions. We report Schottky diodes made from noble metal oxides, IrO_2 and RuO_2, deposited by ozone molecular beam epitaxy (ozone MBE) with barrier heights near 1.8 eV. These barriers show close agreement across extraction methods and robust to high surface electric fields upward of 6 MV/cm and 60 A/cm^2 reverse current without degradation.

I. INTRODUCTION

β-Ga_2O_3 has been widely studied for applications in high power diodes and switches. Owing to its large critical breakdown field of 8 MV/cm, moderate dielectric constant of 10 ε_0, and moderate electron mobility of 200 cm^2/Vs, β-Ga_2O_3 has a Baliga figure of merit several multiples greater than that of 4H-SiC and GaN.[1,2] This high figure of merit indicates that β-Ga_2O_3 can potentially offer a combination of higher breakdown voltages and reduced on-resistance compared to current SiC and GaN devices. Despite encouraging advancements in edge-termination of β-Ga_2O_3 such as field-plated trench diodes,[3] integration of high-κ dielectrics,[4,5] p-n NiO–Ga_2O_3 junctions,[6] and the influence of air exposure on uniform breakdown,[7] intrinsic breakdown has not yet been observed in Ga_2O_3. For unipolar Schottky diodes (SBDs), Li *et al.* have argued that a minimum barrier height of 2.2 eV is necessary to reach 6 MV/cm when defining the breakdown voltage when the device passes 100 mA/cm^2 leakage current. A larger 2.6 eV barrier is required to approach 8 MV/cm.[8] Operating kV devices above 100 mA/cm^2 leakage current is likely not a practical approach to reach higher surface fields as this can lead to significant joule

heating and trap generation. Both mechanisms subsequently induce destructive breakdown or shortened device lifetime.

Given a 4 eV electron affinity for β-Ga_2O_3, large barrier heights can only be achieved with large work function metals such as noble metals and some conductive metal oxides. Prior work fabricated diodes with Ir, Ru, Pd, Pt, Ag, Au metals, and their nonstoichiometric conducting oxides.[9] While sputtering these metals in oxygen environments does not yield uniformly stoichiometric metal oxides, they nominally oxidize to IrO_2, RuO_2, PdO, PtO, $Ag^{I}Ag^{III}O_4$, and Au_2O_3. The diodes fabricated exhibited barrier heights in the range of 1.2–1.4 eV for the nonoxidized metals and 1.9–2.1 eV for the oxidized metals. The extracted barriers vary by up to 0.4 eV when extracted from capacitance-voltage measurements (*C-V*) and forward bias measurements (*I-V*).[9] This is evidence that the measured junctions exhibit some spatial non-uniformity in barrier height, as C-V extractions tend to yield an average barrier value and I-V is biased toward lower barrier heights.[10] Furthermore, Ga_2O_3 has been widely reported to be prone to plasma-induced surface damage,[11] which begs whether the metal oxides under study suffered from any surface damage during deposition. This effect is further observed in sputtered NiO–Ga_2O_3 heterojunction diodes which exhibit significantly reduced barriers due to interface recombination and multistep tunneling.[12,13]

Destructive failure of power diodes is often observed at the edge of metal contacts due to the combined effect of defect-induced field enhancement and edge field crowding.[3] This is corroborated by a study of air exposure to freshly etched Ga_2O_3. By minimizing adsorbed oxygen species and the resulting surface reconstruction, devices exhibited enhanced breakdown voltage and more uniform ablation along the anode edge.[7] Studies of inductively coupled plasma (ICP) and Cl-based etching of Ga_2O_3 also show significantly increased leakage current and the introduction of electrically active defect levels near the surface, respectively.[11,14] Taken collectively, these studies indicate that energetic sputter deposition to date might not only induce significant surface damage and degrade breakdown characteristics but also inhibit studies of large barrier height diodes and high-field behavior in Ga_2O_3. For the diodes in this study, it is notable that the Schottky interface was never exposed to energetic plasma nor Cl-based etching with exception of the PtO_x diode, which was only exposed during the sputter deposition of PtO_x.

Oxide semiconductors, especially those with low-symmetry crystal structures including β-Ga_2O_3, are prone to oxygen vacancies and surface reconstruction. To counter this, a metallic oxide may be used to provide oxygen at the interface. Noble metal oxides, which already suffer from low oxidation potential, are strongly favored thermodynamically to provide oxygen to partially bonded gallium. This may partially fill interfacial vacancies. This reduction in interface state density may reduce Fermi-level pinning of the barrier height and minimize local nonuniformities which lead to premature destructive failure. Nonetheless, oxidation of noble metals is notoriously difficult to achieve due to their high ionization potential and relatively high electronegativity.[15] In recent years, we have developed growth of various large work function noble metal oxides using molecular beam epitaxy (MBE) with ozone as the oxygen source, further referred to as ozone MBE.[16]

In this work, we have prepared and compared β-Ga_2O_3 Schottky barrier diodes made with ozone MBE IrO_2 and RuO_2 to sputtered PtO_x. The temperature-dependent Schottky barrier heights for all three devices are extracted using capacitance-voltage (*C-V*), forward current-voltage (*I-V*), and reverse current density-surface electric field (*J-E*) measurements. Temperature was defined and controlled by a resistive chuck heater and is not corrected for Joule heating at high current. We find that the extracted barrier heights of ozone MBE IrO_2 and RuO_2 show closer agreement than sputtered PtO_x, which has similar variation to prior literature,[9] and are able to withstand significantly higher electric fields and reverse current densities.

II. EXPERIMENT

The vertical SBDs in this study were fabricated on Sn-doped ($\bar{2}01$) edge-defined film-fed growth (EFG) single crystal wafers produced by Novel Crystal Technologies, Inc. The fabrication steps are shown in Fig. 1. The as-received 650 μm thick wafer was diced and cleaned in acetone and isopropanol before soaking in HF and HCl for 5 min each to remove surface imperfections due to wafer polishing and storage. Substrates for sputtered PtO_x and ozone MBE IrO_2 and RuO_2 then have back cathodes formed by deposition of Ti/Pt (75/150 nm) and rapid thermal annealing at 470°C for 1 min in N_2 ambient. At this step, shown in Figs. 1(a) and 1(a′), all three samples are identical.

The two samples for ozone MBE-growth were each loaded into a MBE chamber for blanket deposition of IrO_2 or RuO_2 films, respectively. These films were each grown in a Veeco Gen10 MBE system in a background pressure of $1-3\times10^{-6}$ Torr consisting of 80% distilled ozone as the oxidant. The substrate temperatures for growth were 300° C for the IrO_2 sample and 320° C for RuO_2. Molecular beams of iridium and ruthenium atoms were generated from electron beam evaporation of elemental iridium and ruthenium. X-ray reflectivity (XRR) was used to determine that 28 nm of IrO_2 and 34 nm of RuO_2 were deposited on each sample, respectively. Before capping the metal oxides, Hall measurements were performed to determine carrier density and metallic behavior. 50 nm of Pt or Ru were then deposited by electron beam evaporation on IrO_2 and RuO_2, respectively. These capping layers create an equipotential surface for the electrical contact and provide robustness to probing. Due to equipment limitations, Pt was substituted for Ir as IrO_2's capping layer due to being a similarly noble conductive metal, though it exhibited weak adhesion to IrO_2. Anodes of 100 μm diameter were then created by photolithography, shown in Fig. 1(c′), and mesa isolation via ion milling, shown in Fig. 1(d′), to a depth of 300 nm into the substrate. After electrical measurement, scanning transmission electron microscopy (STEM) samples were prepared using the Thermo Fisher Helios G4 UX Focused Ion Beam with a final milling step of 5 keV. STEM measurements were taken with an aberration-corrected Thermo Fisher Spectra 300 CFEG operated at 300 keV. The cross-sectional samples were extracted from the devices measured and peripheral areas which were never electrically stressed.

The sputtered PtO_x diode was fabricated following the same process flow detailed in Li *et al.*[8] and Saraswat *et al.*[17] After photolithographic definition of the 120 μm diameter anode, shown in

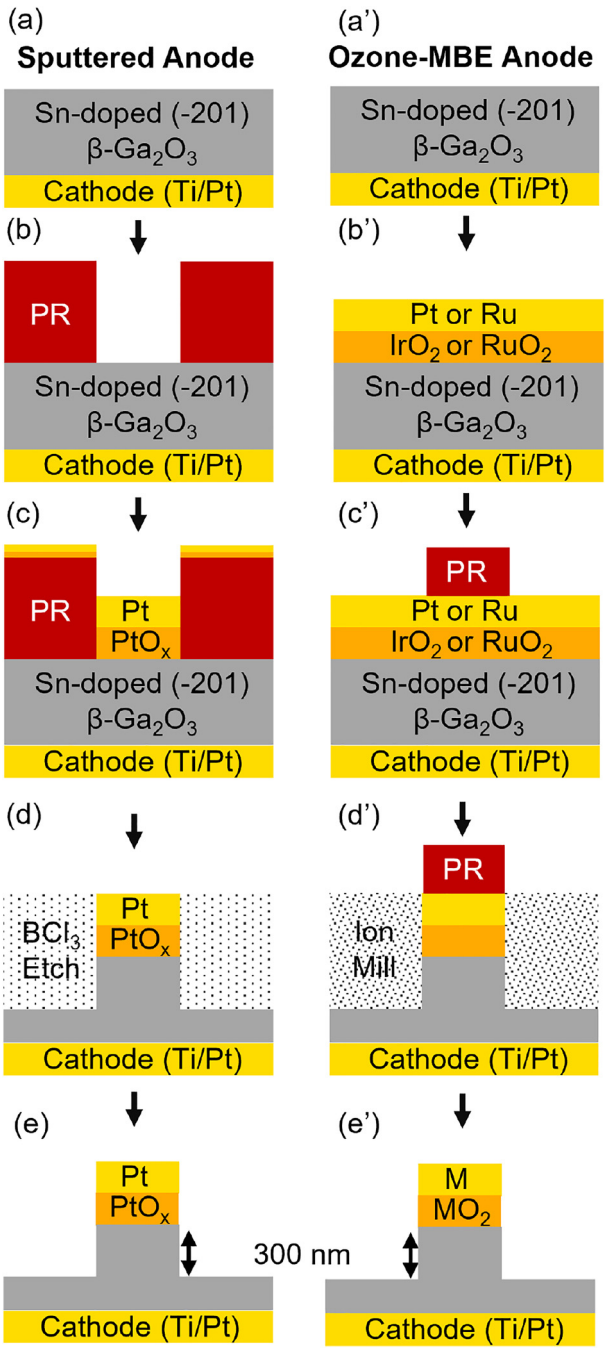

FIG. 1. Schematic of processing of sputtered PtO_x [(a)–(e)] and ozone MBE IrO_2 and RuO_2 [(a′)–(e′)]. Both processes start with annealed Ti/Pt cathode contacts [(a) and (a′)]. The sample for sputtered PtO_x was then patterned with photoresist (PR) (b), before sputter deposition (c), and postliftoff mesa isolation by Cl-based plasma (d). In contrast, the samples for ozone MBE IrO_2 and RuO_2 had anode contacts deposited by MBE then e-beam evaporation (b′) prior to photoresist (PR) patterning (c′) and mesa isolation by Ar^+ ion milling (d′). Both processes result with mesa isolated diodes of mesa height of 300 nm [(e) and (e′)].

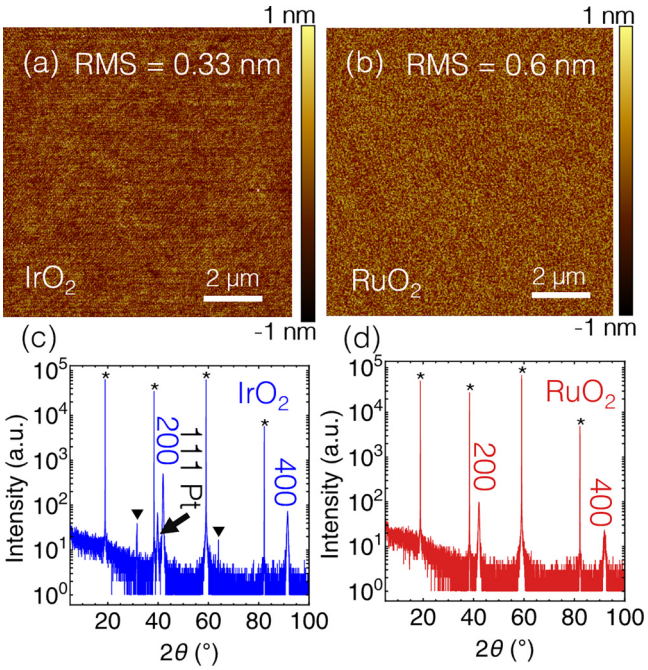

FIG. 2. Large area 100 μm^2 AFM images of (a) IrO_2 and (b) RuO_2 films. XRD establishing that the films are (c) (100)-oriented IrO_2 and (d) (100)-oriented RuO_2. XRD of the IrO_2 sample was captured after SBD fabrication and, thus, shows additional peaks for Pt and γ-Ga_2O_3 possibly induced by the mesa etch. γ-Ga_2O_3 peaks are indicated with a black triangle. Peaks labeled with an asterisk correspond to the reflections arising from the (−201) planes of the β-Ga_2O_3substrate.

Fig. 1(b), 30 nm of PtO_x was deposited with a reactive sputtering process at a gas ratio of $Ar:O_2$=15:15 SCCM. 50 nm of Pt was subsequently deposited by adjusting the $Ar:O_2$ gas ratio to 30:0 SCCM without breaking vacuum. The photoresist was then removed and a self-aligned mesa isolation was created by BCl_3 etch, as shown in Fig. 1(d). As-deposited Pt/PtO_x SBDs exhibited Schottky interface instability previously observed in Ni/β-Ga_2O_3 diodes.[18] A postmetallization anneal (PMA) was performed subsequently at 200° C under N_2 ambient for 10 min and the instability was removed. Since this instability was not observed in the ozone MBE diodes, PMA was not performed. Scanning transmission electron microscopy (STEM) was used to image the PtO_x/Ga_2O_3 interface in peripheral nonelectrically stressed regions. Destructive breakdown was significant enough that STEM of electrically stressed PtO_x/Ga_2O_3 interface was not captured.

III. RESULTS AND DISCUSSION

The electrical and structural properties of the metal oxide films grown by ozone MBE were captured by Hall effect measurements, atomic force microscopy (AFM), and x-ray diffraction (XRD). Hall effect measurements and AFM images were captured prior to deposition of the equipotential Pt or Ru. Indium-based

solder was soldered to the corners of the 10 mm square samples to create a Van der Pauw structure. The indium was completely dissolved in HCl prior to applying the capping layer and photolithographic definition. Both IrO_2 and RuO_2 exhibited metallic carrier densities of 1.18×10^{22} and 1.39×10^{22} cm^{-3} and low resistivities of 0.109 and 0.155 mΩcm, respectively. Notably, both metallic oxides exhibit *positive* Hall coefficients which indicate majority hole carrier type. The mobility of the IrO_2 film was 4.85 and 2.83 cm^2/Vs for RuO_2. 100 μm^2 AFM scans and XRD between 5° and 100° are shown in Fig. 2. The AFM characterization of IrO_2, Fig. 2(a), and RuO_2, Fig. 2(b), shows smooth film surfaces with a root mean square (RMS) roughness of 0.33 and 0.60 nm, respectively. XRD of both ozone MBE films show the film (n00) planes are parallel to the $(\bar{2}01)$ β-Ga_2O_3 planes. Only the (n00) peaks of IrO_2 and RuO_2 are revealed in the large 2θ scan. Thus, there were no parasitic phases or orientations found parallel to the $[\bar{2}01]$ Ga_2O_3 surface normal. The 2θ XRD scan of IrO_2 shown in Fig. 2(c) exhibits additional peaks for the elemental platinum capping layer and γ-Ga_2O_3, a defect spinel structure possibly induced from ion-milling.

Room temperature $1/C^2$–V behavior and doping profile of the PtO_x, IrO_2, and RuO_2 diodes under study are shown in Fig. 3. Since the $1/C^2$–V behavior, shown in Fig. 3(a), is defined by Eq. (1), where $\varepsilon_s = 10\varepsilon_0$ and N_d and ϕ_B are fitting parameters, we are able to extract the barrier height from the x-intercept and carrier density from the slope of $1/C^2$–V response. Further, we can manipulate the derivative of Eq. (1) with respect to voltage, shown in Eq. (2), to yield an expression which relates the capacitance at any given voltage to a doping density N_d. Utilizing Eq. (3) to calculate the depletion width x_d at a given capacitance, we then create the doping profile shown in Fig. 3(b) from the captured $1/C^2$–V. For this model, the diode area is treated as a constant, leaving the applied voltage as the independent variable and the barrier height and doping density as the two fitting parameters. The extracted room temperature barrier heights and mobile carrier densities (N_d–N_a) were 2.25 eV and 7.48×10^{18} cm^{-3} for PtO_x, 1.75 eV and 7.86×10^{18} cm^{-3} for IrO_2, and 1.71 eV and 6.21×10^{18} cm^{-3} for RuO_2,

$$\frac{1}{C^2} = \frac{-2}{qN_d\varepsilon_s A^2} V_a + \frac{2}{qN_d\varepsilon_s A^2} \phi_B, \tag{1}$$

$$N_d(C, V) = \frac{-2}{qN_d\varepsilon_s A^2 \frac{d\frac{1}{C^2}}{dV_a}}, \tag{2}$$

$$x_d(C) = \frac{\varepsilon_s A}{C}. \tag{3}$$

In this study, we utilize three independent methods of determining Schottky barrier height as a function of temperature up to 200°C: zero-capacitance voltage extracted from capacitance-voltage (C-V) measurements, Thermionic Field Emission (TFE) model fit to forward I-V measurements, and numerical tunneling model, developed by Li *et al.*,[8] fit to the reverse J-E measurements.

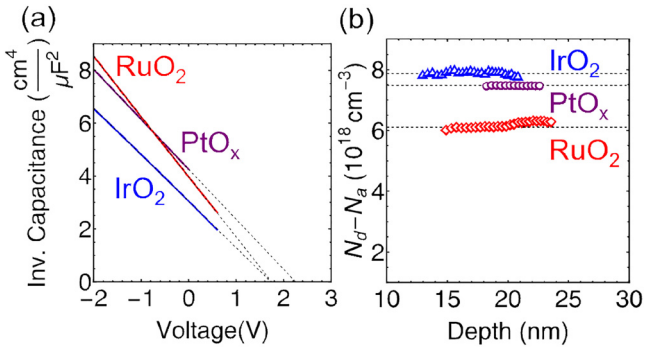

FIG. 3. (a) $1/C^2$–V plots of sputtered PtO_x, IrO_2, and RuO_2 diodes. The extracted barrier heights are 2.27, 1.92, and 1.82 V for PtO_x, IrO_2, and RuO_2, respectively. (b) The extracted carrier profile is shown to be 7.48×10^{18}, 7.86×10^{18}, and 6.21×10^{18} cm^{-3} for the PtO_x, IrO_2, and RuO_2, respectively, with no dispersion toward the surface.

We first recognize that the apparent surface electric field near zero bias is high enough to exceed the crossover field, where thermionic emission (TE) and field emission (FE) are equal.[19] Hence, the forward characteristics of all three Schottky contacts were modeled with the thermionic field emission (TFE) model described by Padovani and Stratton.[20] Utilizing the conventional TE model would attribute reverse leakage current to emission over a lower barrier rather than through a larger barrier. The utilized TFE model described by Padovani and Stratton is detailed in Eqs. (4)–(8), where A^* is the Richardson's Constant for Ga_2O_3, N_c is the effective density of states near the conduction band edge, and $F_{1/2}$ is the Fermi–Dirac integral of order $\frac{1}{2}$. For each temperature, the doping density is taken from the C-V extraction of barrier height, leaving voltage as the independent variable and the barrier height as the only fitting parameter,

$$J_{TFE} = J_{0,\,TFE} \times \exp\left(\frac{qV_a}{E_0}\right), \tag{4}$$

$$J_{0,\,TFE} = \frac{A^* T \sqrt{\pi E_{00}(q\phi_B - \Delta E_{c,\,f} - qV_a)}}{k_B \cosh(E_{00}/k_B T)} \times \exp\left(-\frac{\Delta E_{c,\,f}}{k_B T} - \frac{q\phi_B - \Delta E_{c,\,f}}{E_0}\right), \tag{5}$$

$$E_{00} = \frac{q\hbar}{2}\sqrt{\frac{N_d}{m^*\varepsilon_s}}, \tag{6}$$

$$E_0 = E_{00}\coth\left(\frac{E_{00}}{k_B T}\right), \tag{7}$$

$$N_d = N_c \frac{2}{\sqrt{\pi}} F_{1/2}\left(-\frac{\Delta E_{c,f}}{k_B T}\right). \quad (8)$$

The reverse leakage current was similarly characterized with the numerical tunneling model developed in Li *et al.*[8] This numerical reverse leakage model improves upon the TFE and FE processes described by Murphy and Good, then subsequently by Padovani and Stratton, by including not only doping effects but also image force lowering.[20,21] The total reverse leakage current is given by Eqs. (9)–(12), where E is the electron energy, E_{Fm} is the Fermi-level energy of the metal, E_{min} is the minimum energy for tunneling to occur, x_1 and x_2 are the classical turning points where the conduction band potential is equal to the electron energy $E_c(x) = E$, and $\mathcal{E}$ is the surface electric field. For this model at each temperature, the doping density is again taken from the *C-V* extraction, leaving the voltage, transformed to surface field by Eq. (13), as the independent variable and the barrier height as the only fitting parameter,

$$J = \frac{A^* T}{k_B} \int_{E_{min}}^{+\infty} T(E) \times \ln\left[1 + \exp\left(-\frac{E - E_{Fm}}{k_B T}\right)\right] dE, \quad (9)$$

$$T(E) = \begin{cases} \left[1 + \exp\left(-\frac{2i}{\hbar}\int_{x_1}^{x_2} p(x)dx\right)\right]^{-1} & \text{if} \quad E \le E_{c,max}, \\ 1 & \text{if} \quad E > E_{c,max}, \end{cases} \quad (10)$$

$$p(x) = -i\sqrt{2m^*(E_c(x) - \mathcal{E})}. \quad (11)$$

If $\mathcal{E}_{min}$ is the zero-energy level, then $E_c(x)$ is given by Eq. (12),

$$E_c(x) = q\phi_B - qEx - \frac{q^2}{16\pi\varepsilon_s x} + \frac{q^2 N_d x^2}{2\varepsilon_s}. \quad (12)$$

Temperature-dependent *C-V*, *I-V*, and *J-E* Schottky barrier heights for PtO_x, IrO_2, and RuO_2 are shown in Fig. 4.[23] Despite the ozone MBE diodes having the capability to withstand significantly more than 100 mA/cm^2 reverse current, the region fitted for all devices was limited to below 100 mA/cm^2 for practical comparison to the sputtered PtO_x. It is important to note that *C-V* extractions of barrier height typically are higher than from *I-V*, as seen in the sputtered PtO_x at room temperature. Since *C-V* barrier heights are determined by separated charge across the entire area of the anode, it roughly describes a spatially averaged Schottky barrier height. In contrast, extracting barrier height from current measurements are heavily influenced by regions of lower barrier height which offer the path of least resistance to current flow. Moderate disagreement between the averaged *C-V* barrier and biased *I-V* barrier indicates a spatially nonuniform junction.[10]

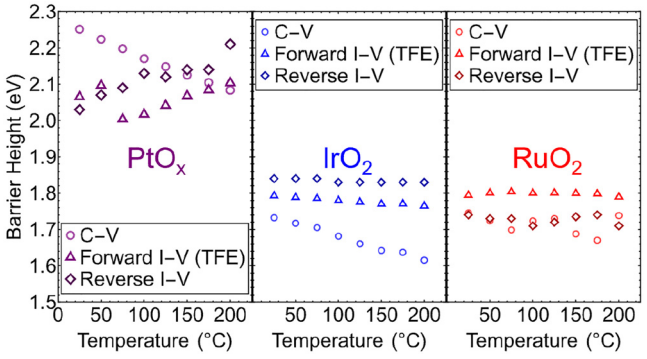

FIG. 4. Extracted *C-V*, forward *I-V*, and reverse *J-E* extractions of Schottky barrier height as a function of temperature for PtO_x (purple), IrO_2 (blue), and RuO_2 (red) SBDs.

PtO_x, despite exhibiting larger barrier heights than the ozone MBE IrO_2 and RuO_2, shows significant disagreement of up to 0.18 eV intramethod and 0.22 eV intermethod, with the closest agreement of 0.06 eV at 175° C. The decrease in *C-V* barrier and increase in *I-V* barriers with temperature are consistent with thermal ionization of deep acceptorlike traps at the Schottky interface. This ionization would both increase the charge per unit area at the anode, thus decreasing the extraction of *C-V* barrier, and enhance the electrostatic barrier observed by electrons thus increasing the *I-V* barrier. This inverse relation of barrier and temperature was also observed by Hou *et al.*[9] Further characterization of the origin and behavior of these interface traps is outside the scope of this study.

In contrast, close agreement of < 0.1 eV is observed between *C-V* and *I-V* barriers of IrO_2 at room temperature and from room temperature to 200° C for RuO_2 diodes. This may indicate that the spatially average barrier height is close to the minimal barrier height for conduction, i.e., a spatially uniform junction.[10] The current-based barrier heights of IrO_2 show minimal deviation with increasing temperature of <0.03 eV intramethod and <0.07 eV intermethod, with the closest agreement of 0.1 eV observed at room temperature. There is a discrepancy in the *C-V* extraction which monotonically decreases with increasing temperature from 1.73 to 1.62 eV. We attribute this decrease to the poor adhesion of the Pt equipotential cap leading to an effective decrease in the area of the diode.[23] RuO_2 similarly shows close agreement with temperature of <0.07 eV intramethod and <0.12 eV intermethod. The closest agreement for RuO_2 of 0.05 eV was observed at room temperature.

The apparent surface electric field describes the electric field near the surface within the depletion region, not accounting for image-force lowering immediate to the Schottky interface. Due to the high substrate doping density and, thus, small depletion region, the electric field within this region is roughly constant and is given by Eq. (13). N_d and $\phi_{B,0}$ are determined from the *C-V* extraction of barrier height at each temperature. *J-E* characteristics allows for direct visualization of maximum apparent surface field withstood by each junction. The apparent surface field is further highlighted in the band diagrams shown in Figs. 5(d) and 5(e),

$$E_{surf} = \sqrt{\frac{2qN_d(\phi_{B,0} - V_a)}{\varepsilon_s}} = \frac{qN_d x_d}{\varepsilon_s}. \quad (13)$$

Figures 5(a)–5(c) show the reverse *J-E* characteristics of all three diodes with overlaid on the numerical tunneling model developed by Li *et al.*, represented by open marks and solid lines,

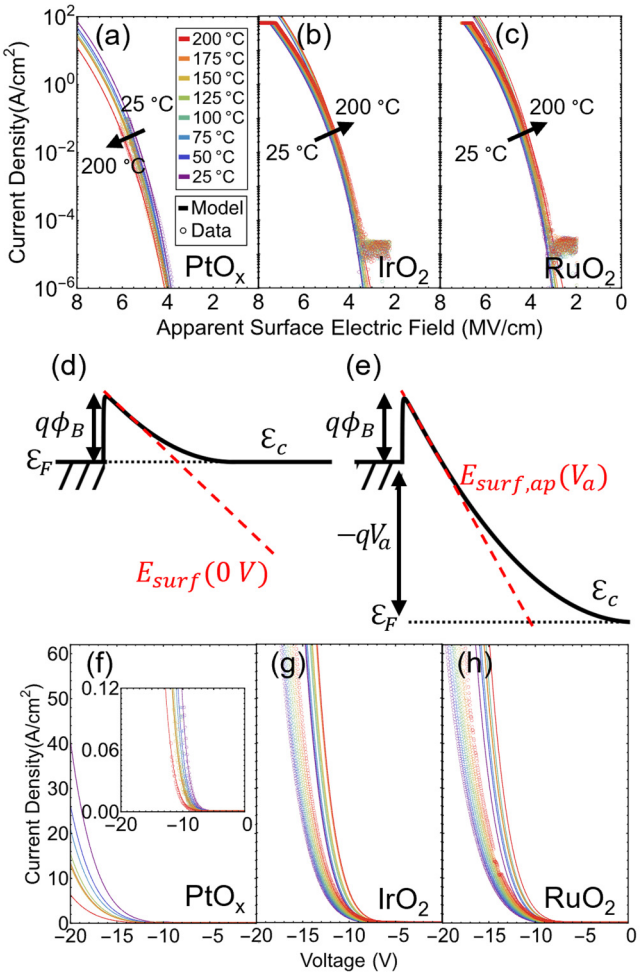

FIG. 5. Reverse *J-E* behavior as a function of temperature for (a) PtO_x, (b) IrO_2, and (c) RuO_2 SBDs. (d) Band diagram of the Schottky barriers at zero bias. (e) Band diagram of the Schottky barriers in reverse bias. Reverse *J-V* behavior is shown in (f)–(h), respectively.The 100 mA/cm^2 limit of PtO_x diodes are shown in the inset of (f) for consistent scaling.

respectively.[8] The apparent surface electric field withstood at 25 and 200°C and at 0.1 and 64 A/cm^2 current densities are summarized in Table I. At 100 mA/cm^2 reverse current density, the apparent surface electric fields 5.68, 5.0, and 4.58 MV/cm for the sputtered PtO_x, IrO_2, and RuO_2. While the sputtered PtO_x exhibited higher apparent surface field at 100 mA/cm^2, the discussed trends of *C-V* and *I-V* barrier heights indicate moderate nonuniformities in the PtO_x Schottky barrier. This is evident from and consistent with the observation that PtO_x diodes were unable to sustain leakage current densities larger than 100 mA/cm^2. PtO_x SBDs cofabricated with the presented device data exhibited significant *nonreversible* degradation of forward and *C-V* characteristics postmeasurement above 100 mA/cm^2 reverse current.

With increasing temperature, PtO_x exhibited *decreased* leakage current attributed to thermally ionized acceptorlike defects at the interface as discussed previously. IrO_2 and RuO_2 exhibit an increase in leakage current, consistent with the numerical tunneling model and prior literature.[8] At 200°C and 100 mA/cm$_2$, the apparent surface electric fields were 6.11, 4.83, and 4.32 MV/cm for PtO_x, IrO_2, and RuO_2, respectively. Though PtO_x was unable to withstand higher current densities, the ozone MBE IrO_2 and RuO_2 were able to sustain reverse leakage current densities greater than 60 A/cm^2 repeatedly on heating and cooling. Reverse *J-V* behaviors of all three devices are shown in Figs. 5(f)–5(h) with the 100 mA/cm^2 limit of the PtO_x shown in the inset of Fig. 5(f).

Above 100 mA/cm^2, the reverse current of the ozone MBE devices deviates from the numerical tunneling model at all temperatures by exhibiting less current than predicted. The disagreement between model and measured increases monotonically to a maximum of 0.6 MV/cm. Since the numerical tunneling model ignores velocity saturation, thermal effects, high-field effects, and non-negligible series resistance, it represents the maximum current and minimum electric field of a diode without realistic limitations. Similar to a forward-biased diode, these limitations will appear in reverse bias at significantly high current density and electric fields. At the maximum current density measured of 64 A/cm^2, the power density varied between 1001 and 1250 W/cm^2 for both ozone MBE diodes at all temperatures. This power density is significant enough to induce joule heating greater than the applied chuck temperature which exacerbates estimations of series resistance and other temperature-dependant effects. Due to lack of *in situ* monitoring or modeling of junction temperature, further discussion of thermal scattering is outside the scope of this study.

Since the numerical tunneling model, calculated using Eqs. (9)–(12), represents the minimum surface field needed to realize a given current density, the minimum apparent surface electric field withstood by each device can be read from the data to the model at a fixed current. Under this scheme, the apparent surface electric fields sustained by the ozone MBE diodes at room

TABLE I. Comparison of the apparent surface electric fields. While the sputtered PtO_x sustain higher apparent surface field at 100 mA/cm^2, they also exhibit significant *nonreversible* degradation postmeasurements and undergo destructive breakdown at reverse currents above 100 mA/cm^2.

$J_{leakage}$ (mA/cm^2)	$T_{applied}$ (°C)	PtO_x (MV/cm)	IrO_2 (MV/cm)	RuO_2 (MV/cm)
100	25	5.68	5.0	4.58
100	200	6.11	4.83	4.32
64	25	N/A	6.94	6.79
64	200	N/A	6.4	6.13

temperature were 6.94 MV/cm in IrO_2 and 6.79 MV/cm in RuO_2. At 200°C, the apparent surface electric fields were 6.4 MV/cm for IrO_2 and 6.13 MV/cm for RuO_2. Apparent surface electric fields of all devices at both 100 and 64 A/cm^2 are summarized in Table I.

Ga_2O_3 power diodes reported to date often fail destructively under a reverse bias current near 100 mA/cm^2 or reverse bias power dissipation around 100 W/cm^2, which can be attributed to time-dependant dielectric breakdown or significant interfacial defects induced by surface reconstruction or vacancies.[7] Leakage and field-enhancement at these defects lead to nonrecoverable damage and ultimately ablative device failure.[7] By electrical measurement, ozone MBE diodes demonstrate interfaces of high enough quality to withstand leakage current far exceeding this value. By consequence, the IrO_2/Ga_2O_3 and RuO_2/Ga_2O_3 interfaces sustain electric fields upward of 6 MV/cm without accumulating critical concentrations of killer defects. Recent analysis utilizing depth-resolved cathodoluminescence (DRCLS) implies this may also be due to the anode structure itself, in that high-field induced electromigration of Ni in a Ni/Ga_2O_3 diode was correlated with defect γ-Ga_2O_3 generation and onset of destructive breakdown.[22] Stoichiometric metal oxide contacts, in this instance, may provide resistance to electromigration due to additional bond character. To examine this hypothesis, high-angle annular dark-field scanning electron microscopy (HAADF-STEM) images of the PtO_x, IrO_2, and RuO_2 interfaces along the [010] zone axis to the $(\bar{2}01)$ surface are shown in Fig. 6.

HAADF-STEM images were first captured at interfaces where no external bias was applied, shown in Fig. 6(a) for PtO_x, Fig. 6(b) for IrO_2, and Fig. 6(c) for RuO_2. The interfacial width between the semiconductor and conductive oxide exhibits a subnanometer transition region. γ-Ga_2O_3 is not observed at the interfaces of any of the structures investigated. In Fig. 6(a), the sputtered PtO_x interface shows increased crystallinity and ordering signified by the elevated contrast relative to the bulk PtO_x several nanometers above the interface. This contrast is attributed to beam channeling along crystalline lattice. Above the interface, randomly orientated PtO/Pt grains 3–8 nm in size comprise the bulk of the PtO_x contact. Similar to Ni, at high field, Pt may diffuse into Ga_2O_3, sourced through diffusion along grain boundaries which have a nonzero cross section with a vertical applied field.[22]

In contrast, the ozone MBE rutile IrO_2 and RuO_2 exhibit atomistically sharp interfaces and uniform vertical columnar structure, corroborating the (n00) ‖ $(\bar{2}01)$ β-Ga_2O_3 relation shown via XRD. The two dominant projection axes of the rutile structure are shown in Fig. 6(d). Rotating from the [001] to [101] projection axes show a FCC-like and pseudocubic structure normal to the Ga_2O_3 interface, indicated by red and blue insets, respectively. Due to these columns having uniform and complete oxidation as well as grain boundaries with zero cross-sectional area to the vertical applied field, diffusion of Ir and Ru, respectively, may be significantly reduced. Reduced metal diffusion would then suppress seeding of breakdown-correlated γ-Ga_2O_3 and other interstitial defects. This is further evidenced by the IrO_2 and RuO_2 interfaces shown in Figs. 6(e) and 6(f). These interfaces, which withstood more than 6 MV/cm electric field, appear as sharp as the unstressed interfaces and retain the columnar structure. This is direct evidence that the Schottky interface remains of high-quality despite high field and temperature cycling up to 200°C.

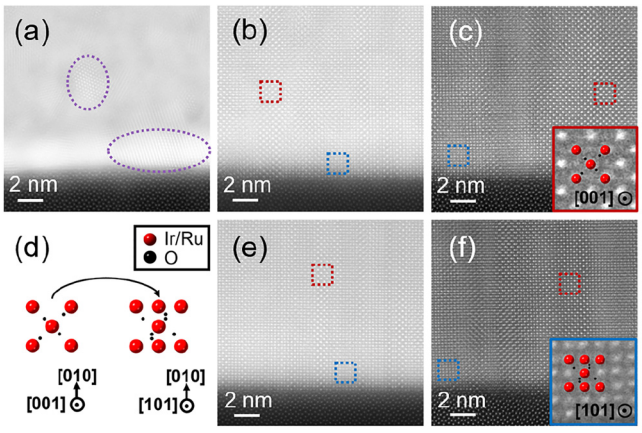

FIG. 6. HAADF-STEM images of as-deposited and unmeasured (a) PtO_x, (b) IrO_2, and (c) RuO_2 Schottky interfaces. All interfaces imaged are aligned to the [010] zone axis of $(\bar{2}01)$ β-Ga_2O_3. Along this zone axis, the rutile IrO_2 and RuO_2 appears primarily along the [001] and [101] projection axes shown in (d). Regions of each projection axis within IrO_2 and RuO_2 are highlighted in red and blue insets. Nanometer-scale grains within PtO_x are highlighted in purple. After electrically stressing to 64 A/cm^2 and above 6 MV/cm, additional HAADF-STEM images of the (e) IrO_2 and (f) RuO_2 interfaces were captured, exhibiting no discernable changes.

IV. SUMMARY AND CONCLUSIONS

In summary, we revisit the topic of large barrier height Schottky diodes to Ga_2O_3 with focus on mitigation and suppression of pinning interfacial defects during processing and anode deposition. By utilizing a combination of plasma-free processing, conductive noble metal oxide anode, and low energy molecular beam epitaxy, high quality IrO_2- and RuO_2-based Ga_2O_3 Schottky barrier diodes were fabricated. Atomic force microscopy, x-ray diffraction, and in-plane Hall measurements confirmed that these metal oxide anodes were below 1 nm RMS roughness across large 100 μm^2 area, highly orientated with (n00) planes parallel to the $(\bar{2}01)$ surface, and metallic carrier densities on the order of 10^{22}cm^{-3}. Schottky barrier height was then determined by three independent methods with temperatures ranging from 25 to 200°C. The ozone MBE devices exhibited higher stability and agreement inter- and intra-method with respect to temperature than the sputtered device, which indicates a higher degree of spatial uniformity. Despite exhibited lower barrier heights, the ozone MBE diodes were of sufficient quality to surpass the 100 mA/cm^2 breakdown criterion up to 64 A/cm^2 without exhibiting degradation or electrical properties nor destructive device failure. HAADF-STEM images confirm a sharp and cohesive structure in the ozone MBE materials before and after high apparent surface electric fields.

At the highest current measured, the apparent surface electric field at room temperature were 6.94 MV/cm in IrO_2 and 6.79 MV/cm in RuO_2. At 200°C, the maximum fields were reduced

to 6.4 and 6.13 MV/cm for IrO_2 and RuO_2, respectively. The columnar structure of IrO_2 and RuO_2 combined with their intrinsically high oxidation potential, additional bond character, and low-energy processing enable high quality large barrier height diodes robust to high surface field, high reverse tunneling current, and moderate temperature.

ACKNOWLEDGMENTS

We wish to acknowledge the support of the AFOSR Center of Excellence Program (No. FA9550-18-1-0529). This work was performed in part at the Cornell Center for Materials Research Shared Facilities (CCMR), which are supported through the NSF MRSEC Program (No. DMR-1719875), and the Cornell Nanoscale Science and Technology Facility (CNF), a member of the National Nanotechnology Coordinated Infrastructure (NNCI), which was supported by the National Science Foundation (NSF) (Grant No. NNCI-2025233). This work was also supported by the NSF [Platform for the Accelerated Realization, Analysis, and Discovery of Interface Materials (PARADIM)] under Cooperative Agreement No. DMR-2039380.

AUTHOR DECLARATIONS

Conflict of Interest

The authors have no conflicts to disclose.

Author Contributions

B. Cromer: Conceptualization (lead); Data curation (lead); Formal analysis (lead); Investigation (lead); Methodology (lead); Writing – original draft (lead); Writing – review & editing (lead). **D. Saraswat:** Conceptualization (lead); Data curation (lead); Formal analysis (lead); Investigation (lead); Methodology (lead); Writing – review & editing (equal). **N. Pieczulewski:** Formal analysis (supporting); Writing – review & editing (supporting). **W. Li:** Conceptualization (equal); Supervision (equal). **K. Nomoto:** Investigation (supporting); Supervision (equal). **F. V. E. Hensling:** Data curation (equal); Investigation (equal); Methodology (equal); Writing – review & editing (supporting). **K. Azizie:** Investigation (equal); Methodology (equal). **H. P. Nair:** Investigation (equal); Methodology (equal); Writing – review & editing (equal). **D. G. Schlom:** Investigation (equal); Methodology (equal); Supervision (equal); Writing – review & editing (equal). **D. A. Muller:** Supervision (supporting). **D. Jena:** Supervision (equal). **H. G. Xing:** Supervision (equal); Writing – review & editing (equal).

DATA AVAILABILITY

The data that support the findings of this study are available from the corresponding author upon reasonable request.

REFERENCES

[1]N. Ma, N. Tanen, A. Verma, Z. Guo, T. Luo, H. G. Xing, and D. Jena, Appl. Phys. Lett. **109**, 212101 (2016).
[2]M. Higashiwaki, AAPPS Bull. **32**, 3 (2022).
[3]W. Li, K. Nomoto, Z. Hu, D. Jena, and H. G. Xing, IEEE Electr. Device Lett. **41**, 107 (2020).
[4]Z. Xia *et al.*, Appl. Phys. Lett. **115**, 252104 (2019).
[5]H. Lee, N. K. Kalarickal, M. W. Rahman, Z. Xia, W. Moore, C. Wang, and S. Rajan, J. Comput. Electron. **19**, 1538 (2020).
[6]Q. Yan *et al.*, Appl. Phys. Lett. **118**, 122102 (2021).
[7]Q. He *et al.*, IEEE Electron Device Lett. **43**, 264 (2021).
[8]W. Li, D. Saraswat, Y. Long, K. Nomoto, D. Jena, and H. G. Xing, Appl. Phys. Lett. **116**, 192101 (2020).
[9]C. Hou, R. M. Gazoni, R. J. Reeves, and M. W. Allen, Appl. Phys. Lett. **114**, 033502 (2019).
[10]J. H. Werner and H. H. Guttler, J. Appl. Phys. **69**, 1522 (1998).
[11]J. Yang, S. Ahn, F. Ren, R. Khanna, K. Bevlin, D. Geerpuram, S. J. Pearton, and A. Kuramata, Appl. Phys. Lett. **110**, 142101 (2017).
[12]H. Gong, X. Chen, Y. Xu, Y. Chen, F. Ren, B. Liu, S. Gu, R. Zhang, and J. Ye, IEEE Trans. Electron Devices **67**, 3341 (2020).
[13]H. Luo, X. Zhou, Z. Chen, Y. Pei, X. Lu, and G. Wang, IEEE Trans. Electron Devices **68**, 3991 (2021).
[14]G. Alfieri, A. Mihaila, P. Godignon, J. B. Varley, and L. Vines, J. Appl. Phys. **130**, 025701 (2021).
[15]K. P. Kepp, Chem. Phys. Chem. **21**, 360 (2020).
[16]D. Kuo, H. Paik, J. N. Nelson, K. M. Shen, D. G. Schlom, and J. Suntivich, J. Chem. Phys. **150**, 041726 (2019).
[17]D. Saraswat, W. Li, K. Nomoto, D. Jena, and H. G. Xing, "Very high parallel-plane surface electric field of 4.3 MV/cm in Ga_2O_3 Schottky barrier diodes with PtO_x contacts," in *2020 Device Research Conference (DRC)* (IEEE, New York, 2020), pp. 1–2.
[18]W. Li, K. Nornoto, Z. Hu, D. Jena, and H. G. Xing, "Barrier height stability and reverse leakage mechanisms in Ni/Ga_2O_3 (001) Schottky barrier diodes," in *2019 Device Research Conference (DRC)* (IEEE, New York, 2019), pp. 159–160.
[19]W. Li, K. Nomoto, D. Jena, and H. G. Xing, Appl. Phys. Lett. **117**, 222104 (2020).
[20]F. A. Padovani and R. Stratton, Solid State Electron. **9**, 695 (1966).
[21]E. L. Murphy and R. H. Good, Phys. Rev. **102**, 1464 (1956).
[22]D. Ramdin, H. Huang, S. Dhara, S. Rajan, J. Hwang, and L. Brillson, "Electric field induced defect redistribution at Ni-Ga_2O_3 interfaces," in *The 6th U.S. Gallium Oxide Workshop* (AVS, Buffalo, NY, 2023).
[23]See the supplementary material online for agreements of *C-V* and forward-*I-V* barrier heights with their respective models and demonstration of Pt/IrO_2 adhesion and impact on *C-V* extraction.